Available online at www.eccomasproceedia.org
Eccomas Proceedia SMART (2023) 1381-1392

ECCOMAS
Proceedia

X ECCOMAS Thematic Conference on Smart Structures and Materials
SMART 2023
D.A. Saravanos, A. Benjeddou, N. Chrysochoidis and T. Theodosiou (Eds)

DEVELOPMENT OF AN INNOVATIVE MAGNETORHEOLOGICAL GEARBOX WITH VARIABLE DAMPING FOR ADVANCED POSITIONING CONTROL

JIAN YANG[*], YUYANG ZHANG[†] AND SHUAISHUAI SUN[†]

[*]School of Electrical Engineering and Automation,
Anhui University, Hefei, Anhui Province 230039, China
e-mail:20152@ahu.edu.cn

[†]CAS Key Laboratory of Mechanical Behavior and Design of Materials, School of Engineering Science, University of Science and Technology of China, Hefei, Anhui Province 230026, China
email: sssun@ustc.edu.cn

Abstract. The robotic arm plays an important role in modern industrial manufacturing. In the operation of the robotic arm, overshoots after the preset position and oscillation during the settling stage are two common issues impairing its positioning performance. To this end, this article designs a magnetorheological (MR) gearbox for the robotic arm to improve its positioning performance. Apart from its conventional function of amplifying motor torque to drive the robotic arm, the MR gearbox is capable of varying damping, which helps to reduce the overshoots and the settling time whilst saving the energy consumed by the motor. The variable damping characteristic of the MR gearbox was first testified and a phenomenon model was built to describe it. Then, a model of a robotic arm system installed with the MR gearbox was established. With the designed control algorithms, i.e., varaible damping (VD) control and improved variable damping (IVD) control being applied, the positioning performance of the robotic arm was numerically evaluated under step and pick-and-place trajectories, respectively. Lastly, the positioning performance of the robotic arm was also experimentally evaluated by a testing platform. Both the numerical and experimental evaluations verify that the positioning control performance of the MR robotic arm is significantly improved by the variable damping characteristics of the MR gearbox, with less overshoot, settling time and energy consumption. Besides, VD control and IVD control have the same capability of decreasing overshoot, but the IVD control outperforms VD control in terms of reducing settling time and energy consumption.

Key words: Robotic arm, positioning control, overshoot, settling time, magnetorheological gearbox, variable damping

1 INTRODUCTION

Robotic arms are usually programmable mechanical arms with similar functions to human arms [1-3]. For robotic arms, positioning control performance is highly important as it

Peer-review under responsibility of the organizing committee of SMART 2023.
doi: 10.7712/150123.9910.448488

influences manufacturing accuracy. When a robotic arm is commanded to move from one position to a desired position, the arm often generates an overshoot after passing the desired position; it then oscillates around the desired position until the final settlement. The large overshoots and long settling times in this progress are two common issues that adversely influence the accuracy and efficiency of the robotic arms. After the settling time, the robotic arm may fall under some external disturbance during its stabilization time, which may also influence its positioning performance. Therefore, much attention has been drawn to addressing them for performing a better positioning performance.

An effective method to mitigate the overshoot and reduce settling time is to develop advanced control algorithms for the robotic arm system. For instance, Yin, et al. [4] designed a nonlinear state feedback controller along with energy shaping for a flexible joint robot. The effectiveness in enhancing the residual vibration suppression and reducing the overshoot of the motor position was experimentally verified. Malki et al. [5] desired a Fuzzy PID control for a flexible-joint robotic arm considering the time-varying loads. The variable gains in the controller enable the arm to perform a fast response with less overshoots than its conventional counterpart. Though the advanced controller effectively improves the positioning performance of robotic arms, such improvement is still compromised by the capability of the motor which drives the robotic arm. After the overshoot, the controller commands the motor to output the maximum torque in the reverse direction of the motion to impede the overshoot caused by inertia and pull the robotic arm back to the desired position. However, the maximum torque of the motor is usually limited, which comprises the positioning performance, especially when the robotic arm is heavily loaded or overloaded.

Hence, the method of integrating additional devices that can provide extra braking torque into the robotic arm system has been adopted. One of them is MR dampers, which are smart devices containing MR Fluids (MRF) [6-11]. Ahn et al. [12] developed a pneumatic muscle robotic arm, in which an MR brake was equipped on the joint of the arm, and large damping was implemented to reduce the overshoot and oscillation when the manipulator reaches the desired position.

Although MR dampers can improve the positioning performance of the robotic arm, their bulky structures significantly increase the complexity and cost of the driving system, which is undesirable for practical applications. The driving components of the robotic arm consist of motors and gearboxes, and the gearboxes are indispensable for amplifying the output torque of the motor to drive the robotic arm. Hence, this work aims to develop a gearbox with the capability of varying damping so the robotic arm system can achieve better positioning control performance with no extra MR damper needed. In the reported MR-based gearboxes [13, 14], MR units are used as clutches to engage or disengage the parts in gearboxes so they can work at different gear ratios. In this work, via a minor modification of a commercial gearbox, the designed MR gearbox can work as an MR damper with damping variability in addition to the general function of amplifying torque output. The innovative contribution of this work is summarised as follows:

1. This work innovatively developed a gearbox with the capability of varying damping by integrating MR technology, which has never been reported.
2. The variable damping gearbox was used for the positioning control system of robotic arms, which is much more compact than those positioning control systems with extra bulky MR dampers.
3. An improved variable damping control algorithm was designed to improve the positioning control performance with less overshoot, settling time and energy consumption.

The MR gearbox was prototyped and experimentally characterised. To evaluate its performance, a robotic arm system was built, and three evaluation trajectories and a case were also designed for the robotic arm to trace. Numerical simulation is implemented to verify its capability to reduce the overshoot and settling time of the system. The rest of the article is organised as follows. Section 2 presents the structural design and working principle of the proposed MR gearbox. Its characterisation tests and mathematical modelling are also introduced. As follows, a robotic arm system installed with the MR gearbox is introduced in section 3, and the positioning control performance of the system is numerically evaluated as well. Finally, the conclusion is drawn in section 5.

2 THE DESIGN, CHARACTERISATION AND MODELLING OF THE MR GEARBOX

2.1 The Structural Design and Working Principle

The MR gearbox was modified based on a commercial planetary gearbox with a gear ratio of 5:1 (ATF60S-5, Chengdu After CNC-Technology Co., Ltd.). As shown in Fig. 1(a), the MR gearbox mainly consists of input and output shafts (#6 and 1), a planetary gear set (#4), two bearings (#3), and a casing (#5). The planetary gear set is presented in Fig. 1(b). It comprises a sun gear (#9), four planetary gears (#7), a planetary carrier (#8), and a casing groove (#10). The casing groove with inward-facing teeth is embedded in the internal surface of the casing, and it

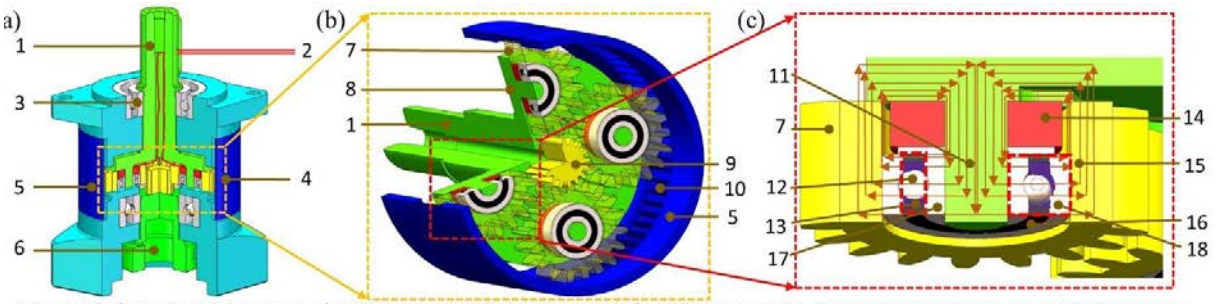

1-Output shaft; 2-Wires; 3-Bearing; 4- Planetary gear set; 5-Casing ; 6-Input shaft; 7-Planetary gear; 8- Planetary carrier; 9-Sun gear; 10-Casing groove; 11-Carrier shaft; 12-MR bearing; 13-MRF; 14-Coil; 15-Magnetic flux circuits; 16-Sealed cap; 17-Inner ring; 18-Outer ring

Fig. 1. Schematic diagram of the MR gearbox.

acts as a ring gear in the planetary gear set. The planetary gears mesh between the sun gear and the casing groove. Meanwhile, as shown in Fig. 1(c), the planetary gears (#7) are connected to the carrier shafts (#11) via MR bearings (#12), with the inner ring (#17) and outer ring (#18) fixed to them, respectively. Different from the conventional gearbox, MRF (#13, MRF-140CG, Lord Corp.) is filled in the bearings, existing in the chamber formed by the inner ring (#17), outer ring (#18) and sealed caps (#16). Additionally, four coils (#14) are also fixed to the carrier shafts, and they are connected in series with the wires (#2, Fig. 1(a)) going out through the hole in the output shaft.

Without current being applied, the MR gearbox acts as a conventional planetary gearbox. Once current is supplied to the coils, magnetic flux circuits (#15) shown in Fig. 1(c) will be induced, which makes the MRF in the bearings transform from the free-flowing state to the half-solid state. Meanwhile, the viscosity of the MRF increases, so the relative motion of the inner and outer rings of the bearings is hindered. Because the inner and outer rings of the bearings are fixed to the planetary carrier shafts and the planetary gears, respectively, the rotation of the planetary gears will be restricted; therefore, the damping of the MR gearbox is increased. By regulating the magnitude of the applied current, the rheological property of the MRF can be controlled, so the damping of the MR gearbox can also be controlled.

2.2 The Characteristication Test

Fig. 3(a) shows the torque-displacement response of the characterization tests. It is observed that, as the current increases from 0 to 1 A, the maximum torque increases 52.04% from 4.58 to 9.55 Nm. Fig. 3(b) presents the equivalent damping coefficient $C_{t,eq}$ at different levels of current, which is calculated by:

$$C_{t,eq} = \frac{EDC}{2\pi^2 f A^2} \tag{1}$$

where $C_{t,eq}$ is the equivalent damping coefficient; EDC is the energy dissipated per cycle which is acquired by calculating the enclosed area of each torque–displacement loop; f is the excitation frequency in Hz; and A is the excitation amplitude. As shown in Fig. 3(a), the enclosed area of torque–displacement loop increases with the increase of current. Fig. 3(b) indicates the calculated equivalent damping coefficient increases of 48.16% from 2.68 to 5.17 N m s rad^{-1} when the current increases from 0 to 1.0A.

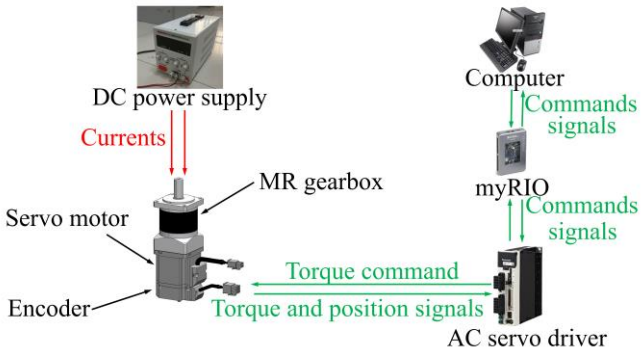

Fig. 2. The schematic of the characteristic test.

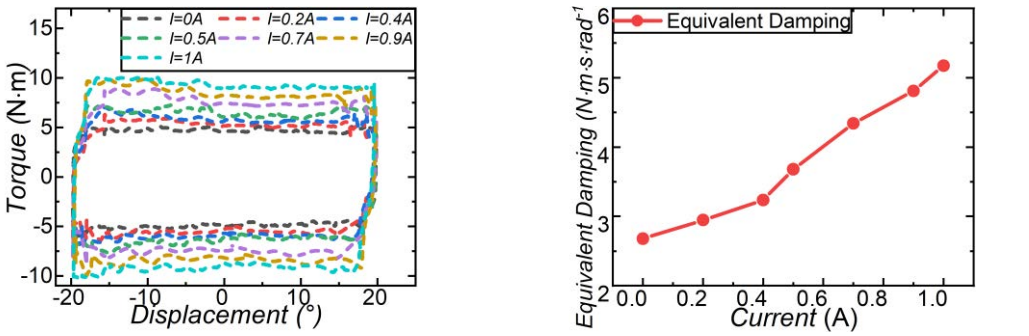

(a) Test results (b) Equivalent Damping coefficient

Fig. 3. The characterization results of the MR planetary gearbox.

2.3 The Mathematical Modeling of the MR Gearbox

As it is revealed in Fig. 3, the MR gearbox behaves similarly to an MR damper with quadratic torque-displacement responses. Hence, the MR gearbox is modelled by the Bouc-Wen model [15], a typical phenomenon model to describe MR damper. The mathematical model of the gearbox is expressed as:

$$T_{vd}(t) = c\,(I)\dot{\varphi}(t) + \alpha(I)z(t) \tag{2}$$

where $T_{vd}(t)$ is the torque output of the gearbox; $\dot{\varphi}(t)$ is the velocity of the output shaft; c(I) is the viscous coefficient, $\alpha(I)$ is a scaling factor, and their relationship to the current I will be established by the parameter identification; $z(t)$ is an evolutionary variable which represents a function of the time history of the displacement, and its governing equation is:

$$\dot{z}(t) = -\gamma|\dot{\varphi}(t)|z|z| - \beta\dot{\varphi}(t)z(t)^2 + A\dot{\varphi}(t) \tag{3}$$

where A, β and γ are constant parameters describing hysteresis behaviour.

To acquire the parameters in Eq. (2) and (3) and enable the model to describe the behaviour of the MR gearbox, the mathematical model was established in MATLAB/Simulink. Then, based on the experimental test results in Fig. 3(a), the parameters were identified by the parameter estimation tool in Simulink with the default nonlinear least-squares method and trust-region reflective algorithm. The principle of this tool is to find the best set of parameters to match the modelled results with the experimental results. The identified variable and constant parameters are presented in Table 1. It is observed that α and c increase with the increase of current, while the rest parameters are constants.

Table 1: Identified Parameters

Current	Variable parameters		Constant parameters		
	α	c	A	β	γ
I=0A	99.9961	0.1028	4.9999	1	26882.807
I=0.2A	108.0971	0.1139			
I=0.4A	117.1873	0.1252			
I=0.5A	127.2899	0.1362			
I=0.7A	138.3746	0.1981			
I=0.9A	146.5392	0.2531			
I=1A	159.468	0.322			

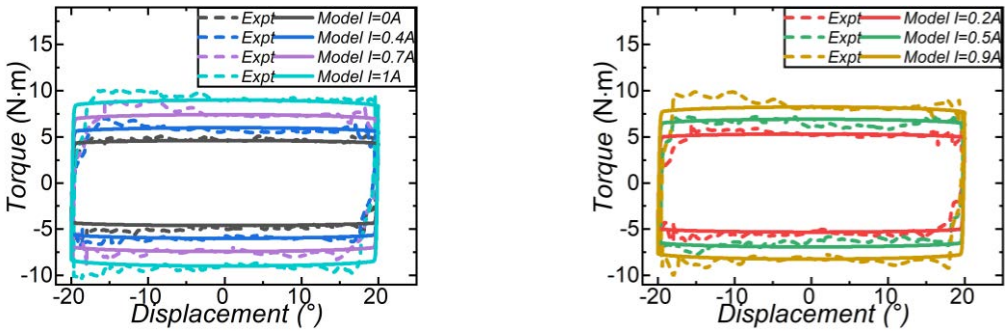

Fig. 4. The results of the modelling

Fig. 4 compares the torque-displacement responses of the modelled results with the experimental results. It is seen that, the modelling results (solid lines) using the established mathematical model and the identified parameters can fit the experimental data (dashed lines) well, indicating a good prediction performance of the proposed model.

3 NUMERICAL EVALUATION OF A ROBOTIC ARM SYSTEM INSTALLED WITH MR GEARBOX

In this section, a robotic arm system is designed to testify the performance of the MR planetary gearbox on the positioning control by numerical simulationThe mathematical model

of the robotic arm system is built at first. Then, three trajectories and a case for the robotic arm to trace and control algorithms to regulate the damping of the MR gearbox are introduced. At last, the positioning control performance of the robotic arm system was evaluated numerically.

3.1 Mathematical Modelling of the Robotic Arm System

The governing equation of the robotic arm system is:

$$J\ddot{\varphi}(t) = 5T_m(t) - T_{VD}(t)\,sign(\dot{\varphi}(t)) - T_f\,sign(\dot{\varphi}(t)) \tag{4}$$

where J= 0.922 kg m2 is the moment of inertia of the robotic arm. $T_m(t)$ is the output torque of the motor, which is magnified by 5 times by the gearbox. T_f is the friction of the system, and its value was set as 0.05 Nm based on the experiment experience. $\varphi(t)$ is the position of the output shaft of the gearbox and the robotic arm. $\dot{\varphi}(t)$ and $\ddot{\varphi}(t)$ are the velocity and acceleration, respectively. The direction of the torque of the gearbox and T_f are always contrary to the motion direction of the robotic arm, so they are multiplied with '-sign($\dot{\varphi}(t)$)'.

In this study, a PID controller with a friction compensation is chosen to drive the motor, so the output torque of the motor $T_m(t)$ is expressed as:

$$\begin{aligned} &T_m(t) = T_{PID}(t) + T_{fc}(t) \\ &and\ T_m(t) \leqslant T_{m\_max} \end{aligned} \tag{5}$$

where $T_{m\_max}=1.91\ Nm$ is the output limitation of the motor.

The output of the PID controller $T_{PID}(t)$ is expressed as:

$$T_{PID}(t) = k_p\varphi_{error}(t) + k_i\int_0^t \varphi_{error}(t)dt + k_d\frac{d(\varphi_{error}(t))}{dt} \tag{6}$$

where k_p= 3, k_i = 0.0001 and k_d = 0.0001 are parameters of the PID controller, and their values are determined by the experimental experience. $\varphi_{error}(t)= \varphi_{design}(t) - \varphi(t)$ is the displacement error between the design position $\varphi_{design}(t)$ and the real-time position of the robotic arm $\varphi(t)$.

$T_{fc}(t)$ in Eq. (5) represents the friction compensation, and it is calculated as

$$\begin{aligned} &T_{fc}(t) = k_f\dot{\varphi}(t) \\ &and\ T_{fc}(t) \leqslant T_{fc\_max} \end{aligned} \tag{7}$$

where k_f and T_{fc_max} are the friction coefficient and the maximum friction. Based on the experiment experience, k_f was set as 0.003 and T_{fc_max} was set as 0.2 N m.

3.2 Evaluation Trajectories and Control Algorithm of the Robotic Arm System

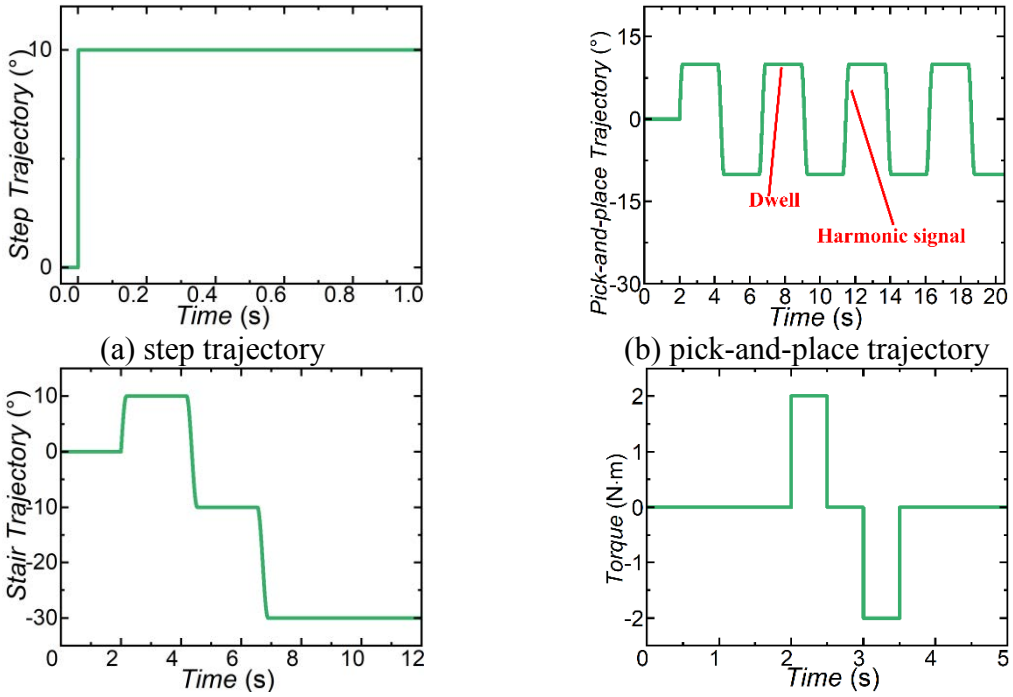

(a) step trajectory (b) pick-and-place trajectory

(c) Stair trajectory (d) External Disturbance

Fig. 6. Evaluation trajectories.

To evaluate the positioning control performance of the robotic arm installed with the MR planetary gearbox, three trajectories shown in Fig. 6(a), (b) and (c) are designed as excitation trajectories for the robotic arm to trace. The first trajectory presented in Fig. 6(a) is a step trajectory, which gives a 10° step at the initial moment t = 0 s to drive the robotic arm to move from 0 to 10°. The second trajectory presented in Fig. 6(b) is a pick-and-place trajectory, which is comprised of the harmonic signal with an amplitude of 10° and a frequency of 1.3 Hz and a two-second dwells arranged at the position of 10° and -10°. The third trajectory is a stair trajectory. This trajectory is used to further test the actual effect of the VD and IVD algorithm. Fig. 6(d) shows the torque applied to the robotic arm. The robotic arm will be applied an external torque during the steady state at two seconds and three seconds to test its ability to reply to the outer disturbance with MR gearbox under PID and IVD algorithms.

These two control strategies are compared in Fig 7, where Fig. 7(a) presents the arm position and Fig. 7(b) presents the corresponding currents of VD and IVD control. In terms of the VD control (whose current is denoted by the blue line), large damping/current (I = 1 A) is constantly applied once the arm position reaches 10°. As indicated by the green dotted line, the IVD control applies large damping/current when the arm position is leaving the target position (Fig. 7 (a)), and applies no current/small damping when the arm position is approaching the target position. With this arrangement, when the arm leaves the target position, the MR gearbox provides extra torque and works with the motor to reduce the overshoot and oscillation; when the arm

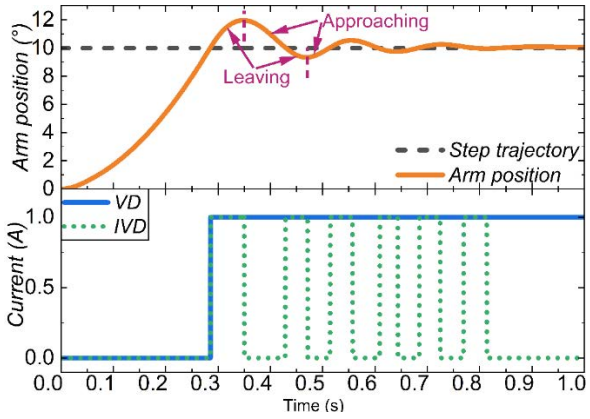

Fig. 7. The working principle of the VD and IVD controllers.

approaches the target position, small damping is applied to avoid the impedance of the robotic arm and save energy.

The IVD control is expressed as:

$$\begin{cases} \dot{\varphi}(t)\,(\varphi(t)-\varphi_{target}(t))>0, \text{ large damping}(I=1)A \\ \dot{\varphi}(t)\,(\varphi(t)-\varphi_{target}(t))<0, \text{ small damping},(I=0)A \end{cases} \tag{8}$$

where $\varphi_{target}(t)$ is 10° or -10°. For the step trajectory, $\varphi_{target}(t)$ is always 10° as it only has one target position. In terms of the pick-and-place trajectory, $\varphi_{target}(t)$ is changing between 10°and -10° along with the time.

3.3. Numerical Evaluation and Result Analysis

The positioning control performance of the robotic arm is numerically evaluated in MATLAB/Simulink module. Three working modes including PID mode, VD mode, and IVD mode were compared. For all working modes, PID control of the motor is working to drive the robotic arm. In the PID mode, the MR gearbox is not controlled. The introduced VD and IVD control are used in the VD and IVD modes, respectively. Under the four trajectories, the positioning control performances of the robotic arm with all working modes were simulated.

Fig. 8 shows the simulation results under four trajectories in terms of the robotic arm position. The overshoot, settling time are summarized in Table 2. Here, the settling time is defined as the time period from the initial to the time at which the oscillation is not exceeding "± 1%" of the target position. The PID mode denoted by the blue lines in Fig. 8 is chosen as an example to illustrate the whole positioning control process.

It is obviously that the overshoot of the PID algorithm is much bigger than PID+VD and PID+IVD. Under the Step Trajectory, the overshoot of the PID mode is 4.581 degree and the PID+VD and PID+IVD have 11.76% reduced. The PID+VD and PID+IVD modes have the same overshoot because large damping is applied to the MR gearbox once the position overtakes 10° for both. The difference is that the large damping will remain for the PID+VD

mode, while for the PID+IVD mode the large damping will only be applied when the arm position is leaving 10°. With this difference, the PID+IVD mode consumes less settling time than PID+VD; compared to the PID mode, the PID+IVD mode reduces 14.73% of the settling time when the PID+VD mode reduces 10.25%. When the robotic arm is working at Pick-and-place Trajectory, with the variable damping characteristics, PID+VD and PID+IVD modes reduce the overshoot, settling time compared to the PID mode. Even though PID+VD and PID+IVD modes perform the same overshoot, the PID+IVD mode works better with less settling time. The above analysis is also supported by the data listed in Table 3. Both PID+VD and PID+IVD modes can reduce the overshoot by 26.23% compared to the normal PID mode, as they both apply large damping once the overshoot happens. The PID+IVD mode consumes the shortest settling time, with 35.09% of settling time being reduced compared to the PID mode. It is observed that, for the three working modes, the arm position of PID mode oscillates much longer than PID+VD and PID+IVD. In the third trajectory, it is observed that the overshoots of PID+VD and PID+IVD modes are largely reduced by 21.26% compared with that of the normal PID mode, and the PID+VD mode is able to reduce the settling time by 34.12%, while the IVD mode can reduce that by 37.57%. When an external torque was applied to the robotic arm, the PID+IVD has a better performance to resist the disturbance with 20.14% reduction of overshoot. To summaries, the variable damping characteristic of the MR gearbox largely reduces the overshoot, settling time of the robotic arm system; the PID+IVD mode works better than the VD mode with less settling time.

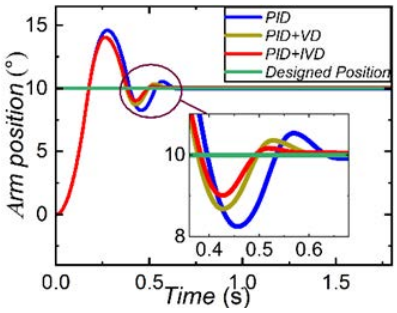

(a) Step Trajectory

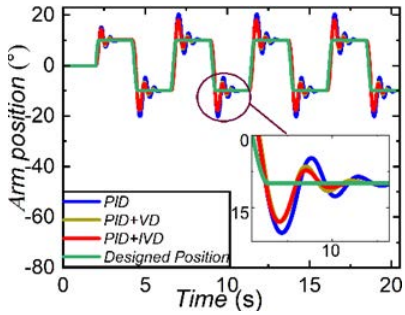

(b) Pick-and-place Trajectory

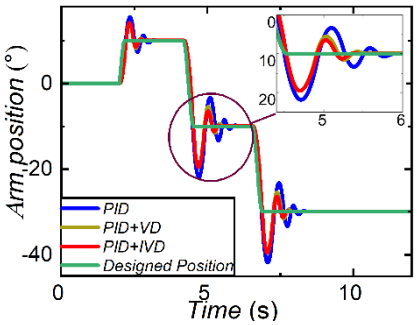

(c) Stair Trajectory

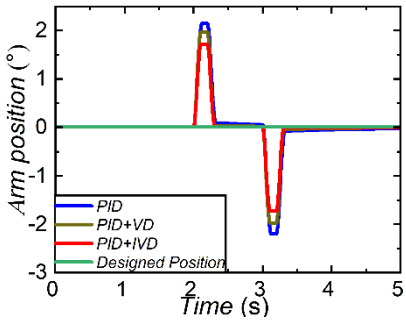

(d) External Disturbance Trajectory

Fig. 8. Simulation results

Table. 2. Data of the simulation results

		PID	PID+VD	PID+IVD
Step Trajectory	Overshoot (°)	4.581	4.042	4.042
	Reduction proportion	NA	11.76%	11.76%
	Settling time (s)	0.663	0.595	0.565
	Reduction proportion	NA	10.25%	14.73%
Pick-and-place Trajectory	Average Overshoot (°)	9.53	7.03	7.03
	Reduction proportion	NA	26.23%	26.23%
	Settling time (s)	1.536	1.225	0.997
	Reduction proportion	NA	20.25%	35.09%
Stair Trajectory	Average Overshoot (°)	9.64	7.59	7.59
	Reduction proportion	NA	21.26%	21.26%
	Settling time (s)	1.392	0.917	0.869
	Reduction proportion	NA	34.12%	37.57%
External Disturbance	Overshoot	2.145	1.968	1.713
	Reduction proportion	NA	8.25%	20.14%

4 CONCLUSION

This paper presented an innovative MR gearbox for improving the positioning performance of the robotic arm. The MR gearbox was designed, prototyped and characterised. Its variable damping capability was verified, and it was found that the maximum torque increased 52.04% from 4.58 to 9.55 Nm and the equivalent damping coefficient increases 48.16% from 2.68 to 5.17 N m s rad^{-1}when the current raised from 0 to 1 A. After establishing the model, the robotic arm installed with the MR gearbox was numerically evaluated under the step， pick-and-place trajectories and stair trajectories. We also designed an experiment to test its performance to resist external disturbance. The simulation results of the step trajectory reveal that the PID+IVD control can reduce 11.76% overshoot and 14.73% settling time compared with the normal PID mode. Similarly, in terms of the pick-and-place trajectory, the average overshoot was reduced by 26.23%, while the average settling time is reduced by 35.09% compared with the PID mode. Under the stair trajectory, PID+VID mode has a reduction of 21.26% with overshoot and 37.57% with settling time, compared with normal PID mode. Under the external disturbance, the PID+IVD mode has a reduction of 20.14% to resist the external disturbance compared with normal PID mode. To sum up, the compact MR gearbox effectively improved the positioning performance via its variable damping characteristics in terms of reducing overshoot, settling time and energy consumption.

REFERENCES

[1] S. De Witte, T. Van Hauwermeiren, T. Lefebvre and G. Crevecoeur, "Learning to Cooperate: A Hierarchical Cooperative Dual Robot Arm Approach for Underactuated Pick-and-Placing," in

IEEE/ASME Transactions on Mechatronics, vol. 27, no. 4, pp. 1964-1972, Aug. 2022, doi: 10.1109/TMECH.2022.3175484.

[2] L. Zhang, T. Xie, S. He, H. Liang, S. Shi, and X. Shan, "A simple linear driving actuator for robotic arm used in land-deep sea," *Mechanical Systems and Signal Processing,* vol. 170, p. 108812, 2022. ISSN 0888-3270, https://doi.org/10.1016/j.ymssp.2022.108812.

[3] Q. Xie, T. Wang and S. Zhu, "Simplified Dynamical Model and Experimental Verification of an Underwater Hydraulic Soft Robotic Arm," *Smart Materials and Structures,* 31, 075011, 2022. DOI 10.1088/1361-665X/ac736f.

[4] W. Yin, L. Sun, M. Wang, and J. Liu, "Nonlinear state feedback position control for flexible joint robot with energy shaping," *Robotics and Autonomous Systems,* vol. 99, pp. 121-134, 2018, doi: 10.1016/j.robot.2017.10.007.

[5] H. A. Malki, D. Misir, D. Feigenspan, and G. Chen, "Fuzzy PID control of a flexible-joint robot arm with uncertainties from time-varying loads," *IEEE Transactions on Control Systems Technology,* vol. 5, no. 3, pp. 371-378, 1997. doi: 10.1109/87.572133.

[6] F. Imaduddin, S. A. Mazlan and H. Zamzuri, "A design and modelling review of rotary magnetorheological damper," *Materials & Design,* vol. 51, pp. 575-591, 2013. https://doi.org/10.1016/j.matdes.2013.04.042.

[7] X. Zhu, X. Jing and L. Cheng, "Magnetorheological fluid dampers: a review on structure design and analysis," *Journal of intelligent material systems and structures,* vol. 23, no. 8, pp. 839-873, 2012. https://doi.org/10.1177/1045389X12436735

[8] R. Ahamed, S.-B. Choi and M. M. Ferdaus, "A state of art on magneto-rheological materials and their potential applications," *Journal of Intelligent Material Systems and Structures,* vol. 29, no. 10, pp. 2051-2095, 2018. https://doi.org/10.1177/1045389X18754350.

[9] G. Liu, F. Gao, D. Wang, and W.-H. Liao, "Medical applications of magnetorheological fluid: a systematic review," *Smart Materials and Structures,* vol. 31, no. 4, 043002, 2022, doi: 10.1088/1361-665X/ac54e7.

[10] J. Huang, S. Li, Y. Zhou, T. Xu, Y. Li, H. Wang, and S. Wang, "A heavy-duty magnetorheological fluid mount with flow and squeeze model," *Smart Materials and Structures,* vol. 30, no. 8, 085012, 2021, doi: 10.1088/1361-665X/ac0673.

[11] X. Deng, X. Dong, J. Xing, W. Li, and J. Xi, "Nonlinear dynamics of magnetorheological whole-satellite with variable parameters under small amplitude and medium-high frequency vibration," *Smart Materials and Structures,* vol. 31, no. 1, 015038, 2021, doi: 10.1088/1361-665X/ac3b1e.

[12] K. K. Ahn and N. H. T. Chau, "Intelligent phase plane switching control of a pneumatic muscle robot arm with magneto-rheological brake," *Journal of mechanical science and technology,* vol. 21, no. 8, pp. 1196-1206, 2007. DOI https://doi.org/10.1007/BF03179036

[13] B.-K. Song, J.-S. Oh and S.-B. Choi, "Design of a new 4-DOF haptic master featuring magnetorheological fluid," *Advances in Mechanical Engineering,* vol. 6, p. 843498, 2014. DOI:10.1155/2014/843498

[14] P. Fauteux, M. Lauria, B. Heintz, and F. Michaud, "Dual-differential rheological actuator for high-performance physical robotic interaction," *IEEE Transactions on Robotics,* vol. 26, no. 4, pp. 607-618, 2010. doi: 10.1109/TRO.2010.2052880.

[15] M. Ismail, F. Ikhouane, and J. Rodellar, "The Hysteresis Bouc-Wen Model, a Survey," *Archives of Computational Methods in Engineering,* vol. 16, no. 2, pp. 161-188, 2009/06/01 2009, doi: 10.1007/s11831-009-9031-8.